

PET-Enabled Dual-Energy CT Using a Kernel Method with Neural Optimization Transfer

Siqi Li, Yansong Zhu, Benjamin A. Spencer and Guobao Wang

Abstract—Integrated use of dual-energy computed tomography (DECT) with positron emission tomography (PET) has many potential clinical applications. However, the integration would either require costly hardware upgrade or increase radiation dose on PET/CT scanners due to the need for an additional X-ray CT scan. The recently proposed PET-enabled DECT method enables DECT imaging on PET/CT without requiring the second X-ray CT scan. It combines the already-existing low-energy X-ray CT image with a 511 keV γ -ray CT (gCT) image reconstructed from time-of-flight PET emission data. A kernelized attenuation and activity (KAA) estimation method has been developed for reconstructing the gCT image from PET but the method has not fully exploited the potential of image prior knowledge. In this work, we propose a neural KAA method by using neural network representation as a deep coefficient prior to improve the existing KAA method. The resulting maximum-likelihood neural network-based reconstruction problem can be efficiently solved by utilizing the theory of optimization transfer. Each iteration of the algorithm consists of three modular steps: PET activity image update, gCT image update, and neural-network learning in the image domain. This algorithm is guaranteed to monotonically increase the data likelihood. The results from computer simulation and real phantom data have demonstrated that the proposed neural KAA method can significantly improve gCT image quality and consequent multi-material decomposition as compared to other methods.

Index Terms—PET-enabled dual-energy CT, PET/CT, image reconstruction, kernel methods, convolutional neural-network

I. INTRODUCTION

CONVENTIONALLY, standard dual-energy computed tomography (DECT) uses two different X-ray energies to obtain energy-dependent tissue attenuation information to allow quantitative multi-material decomposition [1]. Integration of DECT with positron emission tomography (PET) functional imaging enables multi-modality characterization of disease states in cancer and other diseases [2] and would open up novel clinical applications. However, it is not trivial to combine DECT with PET because it either requires costly CT hardware upgrade on existing PET/CT or significantly increases CT radiation dose due to the need for the second X-ray CT scan.

Recently, a PET-enabled DECT method has been proposed to enable DECT imaging on clinical time-of-flight PET/CT scanners without a change of scanner hardware or adding

additional radiation dose or scan time [3]. In PET-enabled DECT imaging, a high-energy “ γ -ray CT (gCT)” image at 511 keV is reconstructed from a standard time-of-flight PET emission scan and combined with the already-existing low-energy X-ray CT (usually < 140 keV) to produce a pair of DECT images for multi-material decomposition.

The gCT image can be reconstructed from PET emission data using the maximum-likelihood attenuation and activity (MLAA) method [5], [6]. However, standard MLAA reconstruction can be very noisy due to the limited counting statistics of PET data. To suppress noise, the kernel MLAA method, or KAA in short in this paper, has been developed by integrating the X-ray CT image prior into the MLAA-based attenuation image reconstruction through a kernel framework [3], [4]. KAA has demonstrated substantial improvements over the MLAA for PET-enabled DECT imaging. Nonetheless the estimated kernel coefficient image may still suffer from noise and result in artifacts in material decomposition, such as in low-count scan cases. The aim of this paper is to develop an improved gCT image reconstruction algorithm for PET-enabled DECT imaging.

Most of current kernel methods for tomographic image reconstruction mainly provide a linear model for image representation, see [7]–[11] for example. On the other hand, deep neural networks offer a more complex nonlinear model for image representation and have been used as deep image prior (DIP) [12] for tomographic reconstruction, as proposed by Gong *et al* [13], [14] and others [15]–[17]. We have recently extended the concept of DIP from the original image space to the kernel coefficient space for the kernelized expectation-maximization (KEM) algorithm for PET activity reconstruction [18]. The resulting neural KEM algorithm has improved over the original KEM or DIP reconstruction for dynamic PET imaging [18].

In this paper, we apply a similar concept to develop a *Neural KAA* approach for PET-enabled DECT imaging by exploiting neural networks as deep coefficient prior for gCT image reconstruction from PET data. One challenge associated with the proposed approach is the complicated optimization that deals with tomographic estimation of neural-network parameters from PET projection data following a maximum-likelihood transmission reconstruction formulation. This is a highly nonlinear and complex problem. We further propose an iterative neural optimization transfer algorithm to address the optimization challenge. The proposed algorithm is easy and efficient to implement in practice by using existing deep learning libraries.

This neural KAA approach is different from other appli-

This work was supported in part by National Institutes of Health (NIH) under grant no. R21 EB027346. Part of this work was presented at the 2021 SPIE Medical Imaging Conference.

S. Q. Li, Y. S. Zhu, and G. B. Wang are with the Department of Radiology, University of California Davis Health, Sacramento, CA 95817, USA. (e-mail: sqlli@ucdavis.edu, yszhu@ucdavis.edu, gbwang@ucdavis.edu).

B. A. Spencer is with the Department of Biomedical Engineering, University of California at Davis, Davis, CA 95616, USA. (e-mail: bspencer@ucdavis.edu)

cations of deep neural networks for MLAA reconstruction [19], [20], which typically target post-reconstruction image processing and require a large database for training. Similar to the original KAA method [3], the neural KAA method has the advantages of not requiring a large training dataset but being directly applicable to single subjects.

The remaining of this paper is organized as follows. Section II introduces the background materials regarding PET-enabled dual-energy CT. Section III describes the proposed neural KAA method for gCT image reconstruction from time-of-flight PET data. The proposed neural optimization transfer algorithm is elaborated in Section IV. We then present a computer simulation study in Section V and a real phantom study in Section VI to demonstrate the improvement of the proposed method. Finally, discussions and conclusions are drawn in Sections VII and VIII, respectively.

II. PET-ENABLED DUAL-ENERGY CT

A. Statistical Model of PET Emission Data

The PET-enabled DECT method exploits the 511 keV gCT image reconstructed from time-of-flight PET emission data \mathbf{y} for dual-energy imaging. Commonly the PET measurement is well modeled as independent Poisson random variables which follows the log-likelihood function:

$$L(\mathbf{y}|\boldsymbol{\lambda}, \boldsymbol{\mu}) = \sum_{i=1}^{N_d} \sum_{m=1}^{N_t} y_{i,m} \log \bar{y}_{i,m}(\boldsymbol{\lambda}, \boldsymbol{\mu}) - \bar{y}_{i,m}(\boldsymbol{\lambda}, \boldsymbol{\mu}), \quad (1)$$

where i denotes the index of PET detector pair and N_d is the total number of detector pairs. m denotes the m th time-of-flight bin and N_t is the number of time-of-flight bins. The expectation of the PET projection data $\bar{\mathbf{y}}$ is related to the radiotracer activity image $\boldsymbol{\lambda}$ and object attenuation image $\boldsymbol{\mu}$ at 511 keV via

$$\bar{\mathbf{y}}_m(\boldsymbol{\lambda}, \boldsymbol{\mu}) = \text{diag}\{\mathbf{n}_m(\boldsymbol{\mu})\} \mathbf{G}_m \boldsymbol{\lambda} + \mathbf{r}_m, \quad (2)$$

where \mathbf{G}_m is the PET detection probability matrix for time-of-flight bin m . \mathbf{r}_m accounts for the expectation of random and scattered events. $\mathbf{n}_m(\boldsymbol{\mu})$ is the normalization factor with the i th element being

$$n_{i,m}(\boldsymbol{\mu}) = c_{i,m} \cdot \exp(-[\mathbf{A}\boldsymbol{\mu}]_i), \quad (3)$$

where $c_{i,m}$ represents the multiplicative factor excluding the attenuation correction factor and \mathbf{A} is the system matrix for transmission imaging.

B. Standard MLAA Reconstruction

The MLAA reconstruction algorithm [5] simultaneously estimates the attenuation image $\boldsymbol{\mu}$ and the activity image $\boldsymbol{\lambda}$ from the PET projection data \mathbf{y} by maximizing the Poisson log-likelihood,

$$\hat{\boldsymbol{\lambda}}, \hat{\boldsymbol{\mu}} = \arg \max_{\boldsymbol{\lambda} \geq 0, \boldsymbol{\mu} \geq 0} L(\mathbf{y}|\boldsymbol{\lambda}, \boldsymbol{\mu}). \quad (4)$$

An iterative interleaved updating strategy is commonly used to seek the solution. At each iteration of the algorithm, $\boldsymbol{\lambda}$ is first

obtained based on the attenuation image $\boldsymbol{\mu}^n$ from the previous iteration n :

$$\boldsymbol{\lambda}^{n+1} = \arg \max_{\boldsymbol{\lambda} \geq 0} L(\mathbf{y}|\boldsymbol{\lambda}, \boldsymbol{\mu}^n), \quad (5)$$

which can be updated by the expectation maximization (EM) algorithm [21] with one subiteration,

$$\boldsymbol{\lambda}^{n+1} = \frac{\boldsymbol{\lambda}^n}{\mathbf{p}^n} \cdot \left(\sum_m \mathbf{G}_m^T \left[\mathbf{n}_m(\boldsymbol{\mu}^n) \cdot \frac{\mathbf{y}_m}{\bar{\mathbf{y}}_m(\boldsymbol{\lambda}^n, \boldsymbol{\mu}^n)} \right] \right), \quad (6)$$

where \mathbf{p}^n denotes the updated sensitivity image from the iteration n , $\mathbf{p}^n = \sum_m \mathbf{G}_m^T \mathbf{n}_m(\boldsymbol{\mu}^n)$.

$\boldsymbol{\mu}$ is then updated with the estimated $\boldsymbol{\lambda}$ following the maximum-likelihood transmission reconstruction formulation,

$$\begin{aligned} \boldsymbol{\mu}^{n+1} &= \arg \max_{\boldsymbol{\mu} \geq 0} L(\mathbf{y}|\boldsymbol{\lambda}^{n+1}, \boldsymbol{\mu}), \\ &= \arg \max_{\boldsymbol{\mu} \geq 0} \sum_{i,m} h_{i,m}([\mathbf{A}\boldsymbol{\mu}]_i), \end{aligned} \quad (7)$$

where

$$h_{i,m}(l) \triangleq y_{i,m} \log(\hat{b}_{i,m} e^{-l} + r_{i,m}) - (\hat{b}_{i,m} e^{-l} + r_{i,m}) \quad (8)$$

with $l = \mathbf{A}\boldsymbol{\mu}$ and

$$\hat{b}_{i,m} = c_{i,m} \cdot [\mathbf{G}_m \boldsymbol{\lambda}^{n+1}]_i. \quad (9)$$

The sub-optimization problem (7) can be solved using the separable paraboloidal surrogate algorithm [22].

Note that conventional applications of MLAA mainly focused on improving PET attenuation correction (e.g., [23]–[28]). Differently in our PET-enabled DECT method, the gCT image $\boldsymbol{\mu}$ is combined with X-ray CT to form a DECT image pair for multi-material decomposition [3].

C. Kernel MLAA (KAA) for gCT Reconstruction

The gCT image estimate by the MLAA method [5] is commonly noisy due to the limited counting statistics of PET emission data. To suppress noise, the kernel MLAA or KAA integrates the X-ray CT prior image into the PET forward model by describing the gCT image intensity μ_j at pixel j using a kernel representation [3], [4],

$$\mu_j = \sum_{l \in \mathcal{N}_j} \alpha_l \kappa(\mathbf{f}_j, \mathbf{f}_l), \quad (10)$$

where $\kappa(\cdot, \cdot)$ is the kernel function (e.g., radial Gaussian) with \mathbf{f}_j and \mathbf{f}_l denoting the feature vectors of pixel j and l that are extracted from the X-ray CT image. \mathcal{N}_j defines the neighborhood of pixel j , for example, selected by a k-nearest neighbor algorithm. α_l denotes the corresponding kernel coefficient of each neighboring pixel l in \mathcal{N}_j .

The equivalent matrix-vector form for the gCT image representation is

$$\boldsymbol{\mu} = \mathbf{K}\boldsymbol{\alpha}, \quad (11)$$

where \mathbf{K} is the kernel matrix and $\boldsymbol{\alpha}$ is the corresponding kernel coefficient image. Substituting (11) into the MLAA formulation in (4) gives the following KAA optimization formulation,

$$\hat{\boldsymbol{\lambda}}, \hat{\boldsymbol{\alpha}} = \arg \max_{\boldsymbol{\lambda} \geq 0, \boldsymbol{\alpha} \geq 0} L(\mathbf{y}|\boldsymbol{\lambda}, \mathbf{K}\boldsymbol{\alpha}). \quad (12)$$

Once $\hat{\alpha}$ is determined, the gCT image is obtained as $\hat{\mu} = \mathbf{K}\hat{\alpha}$. Note that the conventional MLAA can be considered as a special case of the KAA with \mathbf{K} equal to an identity matrix.

The KAA problem is also solved using an interleaving optimization strategy between the activity image λ update and the kernel coefficient image α update [3]. In each iteration of KAA, λ^{n+1} is first obtained using the EM updating formula (6) and then α^{n+1} is obtained using the following kernelized transmission reconstruction (KTR) optimization,

$$\alpha^{n+1} = \arg \max_{\alpha \geq 0} \sum_{i,m} h_{i,m}([\mathbf{A}\mathbf{K}\alpha]_i). \quad (13)$$

An optimization transfer algorithm using the separable paraboloidal surrogate [22] has been derived in [3] for KTR.

D. Material Decomposition Using PET-enabled DECT

For each image pixel j , the gCT attenuation value μ_j and X-ray CT attenuation value x_j jointly form a pair of dual-energy measurements $\mathbf{u}_j \triangleq [x_j, \mu_j]^T$, which can be modeled by a set of material bases, such as air (A), soft tissue (S) or equivalently water, and bone (B):

$$\mathbf{u}_j = \mathbf{U}\boldsymbol{\rho}_j, \quad \mathbf{U} \triangleq \begin{pmatrix} x_A & x_S & x_B \\ \mu_A & \mu_S & \mu_B \end{pmatrix}, \quad \boldsymbol{\rho}_j \triangleq \begin{pmatrix} \rho_{j,A} \\ \rho_{j,S} \\ \rho_{j,B} \end{pmatrix}, \quad (14)$$

subject to $\sum_k \rho_{j,k} = 1$. The coefficients $\rho_{j,k}$ with $k = A, S, B$ are the fraction of each basis material in pixel j . The material basis matrix \mathbf{U} consists of the linear attenuation coefficients of each basis material measured at the low and high energies. Finally, $\boldsymbol{\rho}_j$ is estimated using the following least-square optimization for each image pixel,

$$\hat{\boldsymbol{\rho}}_j = \arg \min_{\boldsymbol{\rho}_j \geq 0} \|\mathbf{u}_j - \mathbf{U}\boldsymbol{\rho}_j\|^2. \quad (15)$$

III. PROPOSED NEURAL KAA

A. Kernel Model With Deep Coefficient Prior for gCT

While demonstrating a substantially better performance than MLAA (e.g., in [3]), KAA may still suffer from noise or artifacts particularly in low-count cases. In this work, we exploit neural networks as a deep coefficient prior for improving KAA for gCT image reconstruction. The kernel coefficient image α in (11) is described as a function of neural networks,

$$\alpha = \psi(\boldsymbol{\theta}|z), \quad (16)$$

where z is the available image prior (e.g., X-ray CT in this work) and ψ denotes the neural network mapping from the input image z to the α image with $\boldsymbol{\theta}$ the parameters of the neural network.

The gCT image is then modeled using the following kernel representation with deep coefficient prior,

$$\mu = \mathbf{K}\psi(\boldsymbol{\theta}|z). \quad (17)$$

Fig. 1(a) shows a graphical illustration of the proposed model for representing a gCT image, of which the last layer is a linear kernel representation with pre-determined weights $\{\kappa_{j,l}\}$ that are also calculated from z . Any neural-network model with the

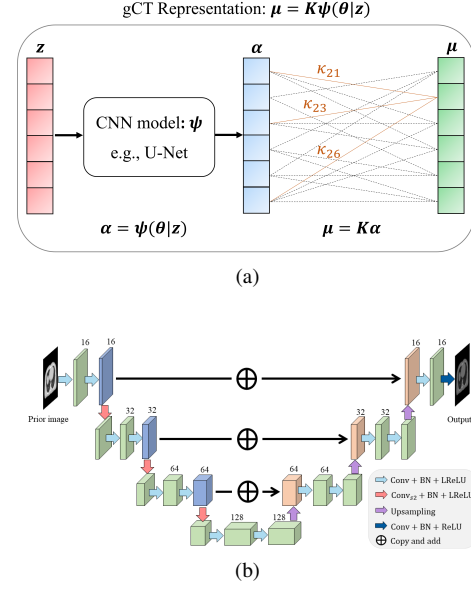


Fig. 1: Graphical illustration of the kernel model with deep coefficient prior for gCT μ representation. An example of the convolutional neural network (CNN) is the residual U-Net $\psi(\boldsymbol{\theta}|z)$.

same size of input and output can be suitable for the proposed image representation. An example is the residual U-Net model that is used in [13], [18], as also shown in Fig. 1(b).

This approach is similar to our neural KEM work that improves dynamic PET activity image reconstruction [18], but here the idea is applied to a transmission reconstruction problem. The model (17) is equivalent to the standard KAA image model in (11) if the neural network ψ is an identity mapping. It is also equal to a DIP model directly in the gCT image domain if the kernel matrix \mathbf{K} is an identity matrix, which leads to $\mu = \psi(\boldsymbol{\theta}|z)$ and shares the same spirit as the work of Gong *et al.* [13] that uses DIP for PET activity image reconstruction.

B. Incorporation in the KAA Framework

By substituting the gCT representation (17) into the MLAA formulation (4), we have the proposed neural KAA using the following optimization formulation,

$$\hat{\lambda}, \hat{\boldsymbol{\theta}} = \arg \max_{\lambda \geq 0, \boldsymbol{\theta}} L(\mathbf{y}|\lambda, \mathbf{K}\psi(\boldsymbol{\theta}|z)). \quad (18)$$

Similar to the optimization approach for MLAA and KAA, an interleaving updating strategy can be used here to estimate λ and $\boldsymbol{\theta}$ iteratively,

$$\lambda^{n+1} = \arg \max_{\lambda \geq 0} L(\mathbf{y}|\lambda, \mathbf{K}\psi(\boldsymbol{\theta}^n|z)), \quad (19)$$

$$\boldsymbol{\theta}^{n+1} = \arg \max_{\boldsymbol{\theta}} L(\mathbf{y}|\lambda^{n+1}, \mathbf{K}\psi(\boldsymbol{\theta}|z)). \quad (20)$$

Once $\boldsymbol{\theta}$ is estimated, the gCT image is obtained by

$$\hat{\mu} = \mathbf{K}\psi(\hat{\boldsymbol{\theta}}|z). \quad (21)$$

Compared to the previous KAA approach, the neural KAA approach combines the kernel representation with a neural network-based deep coefficient prior, which introduces an implicit regularization for KAA to improve the gCT image estimate $\hat{\mu}$ through (20).

C. The Optimization Challenge

In each iteration of the neural KAA, the λ estimation step in (19) can be directly implemented by using the EM algorithm (6). The θ -estimation step (20) follows a KTR formulation but with using neural networks as deep coefficient prior. For simplicity, we rewrite this *neural* KTR problem in (20) as

$$\theta^{n+1} = \arg \max_{\theta} J_n(\theta), \quad (22)$$

where $J_n(\theta)$ is the transmission likelihood function at iteration n ,

$$\begin{aligned} J_n(\theta) &\triangleq L(\mathbf{y}|\lambda^{n+1}, \mathbf{K}\psi(\theta|\mathbf{z})) \\ &= \sum_{i,m} h_{i,m}([\mathbf{A}\mathbf{K}\psi(\theta|\mathbf{z})]_i), \end{aligned} \quad (23)$$

with $h_{i,m}$ defined in (8) but the line integral l following a kernelized neural-network model,

$$l = \mathbf{A}\mathbf{K}\psi(\theta|\mathbf{z}). \quad (24)$$

The optimization problem (22) is challenging to solve because the unknown θ is nonlinearly involved in the projection domain for transmission imaging due to (24), resulting in a complex optimization problem.

One commonly used solution would be a type of gradient descent algorithm that uses the chain rule to calculate the gradient of $J_n(\theta)$ with respect to θ [29]–[31],

$$\frac{\partial J_n(\theta)}{\partial \theta} = \frac{\partial J_n(\theta)}{\partial \psi} \cdot \frac{\partial \psi}{\partial \theta}, \quad (25)$$

which is then fed into an existing deep learning package to estimate the network parameters from the PET projection data \mathbf{y} . However, such an approach ties each calculation of $\frac{\partial \psi}{\partial \theta}$, which relates to the neural network component, with a calculation of $\frac{\partial J_n(\theta)}{\partial \psi}$, which relates to the PET tomographic reconstruction. While the former operation is usually efficient by using a deep learning library, the latter operation requires both forward and back projections of PET data and is computationally intensive due to the large size of the transmission system matrix \mathbf{A} . As a result, the whole algorithm can be slow due to the natural need for many iterations for training a neural network.

In this work, we develop an approach to decoupling the reconstruction step and neural network learning step towards a more practical and efficient implementation of the neural KTR and thus the neural KAA.

IV. A NEURAL OPTIMIZATION TRANSFER ALGORITHM

A. Principle of Optimization Transfer

The proposed algorithm shares the same spirit as the nested optimization transfer algorithms developed for tomographic reconstruction of nonlinear kinetic parameters in dynamic PET [32], [33]. The idea is to use optimization transfer [34] to convert the original difficult problem for $J_n(\theta)$ into a surrogate optimization problem, as illustrated in Fig. 2, for which the surrogate function $\phi_J(\theta|\theta^n)$ minorizes the transmission likelihood function $J_n(\theta)$,

$$\phi_J(\theta|\theta^n) \leq J_n(\theta), \quad (26)$$

$$\phi_J(\theta^n|\theta^n) = J_n(\theta^n). \quad (27)$$

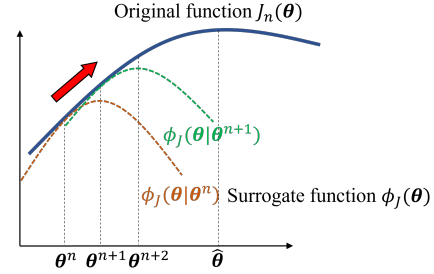


Fig. 2: Graphical illustration of the basic idea of optimization transfer. The surrogate function $\phi_J(\theta)$ minorizes the original objective function $J_n(\theta)$. The new update θ^{n+1} , which achieves the maximizer in $\phi_J(\theta|\theta^n)$, will guarantee a monotonic increase in $J_n(\theta)$ and converge to the local maximum solution $\hat{\theta}$ in the direction of the red arrow.

Then the maximization of $J_n(\theta)$ is transferred into maximizing the surrogate function,

$$\theta^{n+1} = \arg \max_{\theta} \phi_J(\theta|\theta^n). \quad (28)$$

The surrogate $\phi_J(\theta|\theta^n)$ is usually designed to be easy to solve. The new update θ^{n+1} is guaranteed to monotonically increase the original likelihood $J_n(\theta)$, i.e.,

$$J_n(\theta^{n+1}) \geq J_n(\theta^n), \quad (29)$$

as also demonstrated by Fig. 2.

B. Minorization by Paraboloidal Surrogates

One difficulty with dealing the objective function $J_n(\theta)$ directly is the Poisson log-likelihood function follows a non-quadratic form. As already used in the KAA approach, a paraboloidal surrogate function can be constructed for $J_n(\theta)$ [3], [35],

$$\begin{aligned} J_n(\theta) &\geq S(\theta|\theta^n) \\ &= \sum_{m,i} h_{i,m}(l_i^n) + \dot{h}_{i,m}(l_i^n)\Delta l_i - \frac{\eta_{i,m}(l_i^n)}{2}\Delta l_i^2, \end{aligned} \quad (30)$$

where l_i^n is l_i calculated with θ^n and $\Delta l_i = l_i - l_i^n$. $\eta_{i,m}(l)$ is chosen by design as the optimal curvature of the Poisson log-likelihood [35],

$$\eta_{i,m}(l) = \begin{cases} \frac{2}{l^2} [h_{i,m}(l) - h_{i,m}(0) - l\dot{h}_{i,m}(l)], & l > 0 \\ -\ddot{h}_{i,m}(l), & l = 0 \end{cases} \quad (31)$$

where $\dot{h}_{i,m}(l)$ and $\ddot{h}_{i,m}(l)$ are the first and second derivatives of $h_{i,m}(l)$, respectively [35].

With several algebraic operations similar to the way in [32], we then can derive the following equivalent quadratic form for $S(\theta|\theta^n)$ in (30),

$$S(\theta|\theta^n) = -\frac{1}{2} \|\hat{l}^{n+1} - \mathbf{A}\mathbf{K}\psi(\theta|\mathbf{z})\|_{\hat{\eta}_n}^2 + C_S^n, \quad (32)$$

where C_S^n is the remainder that is independent of the unknown parameter θ . \hat{l}^{n+1} is an intermediate gCT projection data [3],

$$\hat{l}_i^{n+1} = l_i^n + \frac{\sum_m \dot{h}_{i,m}(l_i^n)}{\sum_m \eta_{i,m}(l_i^n)}, \quad (33)$$

and $\hat{\eta}^n$ is an intermediate weight also in the projection domain,

$$\hat{\eta}_i^n = \sum_m \eta_{i,m}(l_i^n). \quad (34)$$

Based on this quadratic surrogate $S(\theta|\theta^n)$, the maximization of $J_n(\theta)$ for the neural KTR is transferred to an equivalent weighted least-square reconstruction problem,

$$\hat{\theta}^{n+1} = \arg \min_{\theta} \frac{1}{2} \|\hat{l}^{n+1} - \mathbf{AK}\psi(\theta|z)\|_{\hat{\eta}^n}^2. \quad (35)$$

This quadratic form is simpler than the original non-quadratic likelihood function $J_n(\theta)$. However, the nonlinear neural network model $\psi(\theta|z)$ is still coupled in the projection domain.

C. Minorization by Separable Quadratic Surrogates

By considering \mathbf{AK} as a single matrix and using the convexity of (32) to build a separable quadratic surrogate [36], we can construct the following surrogate $s(\theta|\theta^n)$ for $S(\theta|\theta^n)$,

$$\begin{aligned} S(\theta|\theta^n) &\geq s(\theta|\theta^n) \\ &= S(\theta^n|\theta^n) + (\mathbf{g}^n)^T \Delta\psi(\theta|z) - \frac{1}{2} \|\Delta\psi(\theta|z)\|_{\omega^n}^2 \end{aligned} \quad (36)$$

where $\Delta\psi(\theta|z) \triangleq \psi(\theta|z) - \psi(\theta^n|z)$. \mathbf{g}^n is the gradient of $S(\theta|\theta^n)$ with respect to ψ at iteration n ,

$$\mathbf{g}^n = \mathbf{K}^T \mathbf{A}^T \text{diag}(\hat{\eta}^n) (\hat{l}^{n+1} - \mathbf{AK}\psi(\theta^n|z)), \quad (37)$$

and ω^n is an intermediate weight image,

$$\omega^n = \mathbf{K}^T \mathbf{A}^T \text{diag}(\hat{\eta}^n) \mathbf{AK} \mathbf{1}, \quad (38)$$

where $\mathbf{1}$ is the all-one vector. Note that \mathbf{g}^n is also equal to the gradient of $J_n(\theta)$ with respect to ψ at iteration n .

After a few algebraic operations as also used in [32], we can have the following equivalent form for $s(\theta|\theta^n)$,

$$s(\theta|\theta^n) = \frac{1}{2} \|\hat{\alpha}_j^{n+1} - \psi(\theta|z)\|_{\omega^n}^2 + C_s^n \quad (39)$$

where $\hat{\alpha}^{n+1}$ is an intermediate kernel coefficient image calculated from

$$\hat{\alpha}^{n+1} = \alpha^n + \frac{\mathbf{g}^n}{\omega^n}, \quad (40)$$

with $\alpha^n \triangleq \psi(\theta^n|z)$. C_s^n denotes the corresponding remainder term that is independent of θ . Note that $\hat{\alpha}^{n+1}$ is equivalent to one iteration of the KTR reconstruction algorithm in [3].

Thus, the weighed least-square reconstruction problem (35) defined in the projection domain is transferred to the following neural-network learning problem that is fully defined in the image domain,

$$\theta^{n+1} = \arg \min_{\theta} \frac{1}{2} \|\hat{\alpha}_j^{n+1} - \psi(\theta|z)\|_{\omega^n}^2. \quad (41)$$

In particular, the cost function here follows a weighted l_2 -norm loss that can be easily used with an existing deep learning package (e.g., PyTorch).

It is straightforward to prove that the surrogate function $s(\theta|\theta^n)$ minorizes the original likelihood function $J_n(\theta)$,

$$s(\theta|\theta^n) \leq S(\theta|\theta^n) \leq J_n(\theta), \quad (42)$$

$$s(\theta^n|\theta^n) = S(\theta^n|\theta^n) = J_n(\theta^n). \quad (43)$$

D. Summary of the Algorithm

A pseudo-code of the proposed neural KAA algorithm is summarized in Algorithm 1. The algorithm consists of three separate steps in each iteration:

- 1) **PET activity image reconstruction:** Obtain the PET activity image update λ^{n+1} using the MLEM algorithm in (6).
- 2) **Kernelized gCT image reconstruction:** Obtain an intermediate kernel coefficient image update $\hat{\alpha}^{n+1}$ using one iteration of the KTR algorithm in (40);
- 3) **Least-square neural-network learning for image approximation:** Update the network model parameters θ^{n+1} using (41) to approximate $\hat{\alpha}^{n+1}$;

Step 1 and step 2 are updated analytically. PET projection data are only involved in these two steps. Step 3 can be implemented efficiently using existing deep learning packages without involving any projection data directly. Thus, the neural network learning step is decoupled from the image reconstruction steps and is easy to implement in practice.

Algorithm 1 Neural KAA for gCT reconstruction

- 1: Input parameters: Maximum iteration number `MaxIt`, initial λ^1 , and initial θ^1 to provide $\alpha^1 = \psi(\theta^1|z)$.
 - 2: **for** $n = 1$ to `MaxIt` **do**
 - 3: Obtain the activity image update λ^{n+1} using (6);
 - 4: Get the intermediate kernel coefficient image $\hat{\alpha}^{n+1}$:
 $\hat{\alpha}^{n+1} = \alpha^n + \frac{\mathbf{g}^n}{\omega^n}$,
 where \mathbf{g}^n and ω^n are calculated based on $\hat{\eta}^n$ in (34) and \hat{l}^{n+1} in (33);
 - 5: Perform a neural-network learning to approximate the image $\hat{\alpha}^{n+1}$ using the weighted l_2 -norm loss to update θ^{n+1} and $\alpha^{n+1} = \psi(\theta^{n+1}|z)$:
 $\theta^{n+1} = \arg \min_{\theta} \frac{1}{2} \|\hat{\alpha}_j^{n+1} - \psi(\theta|z)\|_{\omega^n}^2$;
 - 6: **end for**
 - 7: **return** $\hat{\mu} = \mathbf{K}\psi(\hat{\theta}|z)$
-

V. COMPUTER SIMULATION STUDIES

A. Simulation Setup

We first conducted a two-dimensional computer simulation study following the GE Discovery 690 PET/CT scanner geometry. This PET scanner has a time-of-flight timing resolution of approximately 550 ps. The simulation was conducted using one chest slice of the XCAT phantom [37]. Fig. 3a and Fig. 3b show the simulated ground truth of PET activity image and 511 keV gCT attenuation image, respectively. The low-energy X-ray CT image was simulated from XCAT at 80 keV and is shown in Fig. 3c. The activity and gCT images were first forward projected to generate noise-free emission sinograms of 11 time-of-flight bins. A 40% uniform background was included to simulate random and scattered events. Poisson noise was then generated using 5 million expected events. The projection data was reconstructed into PET activity and gCT images of 180×180 with a pixel size of 3.9×3.9 mm². Ten noisy realizations were simulated and reconstructed for comparing reconstruction methods.

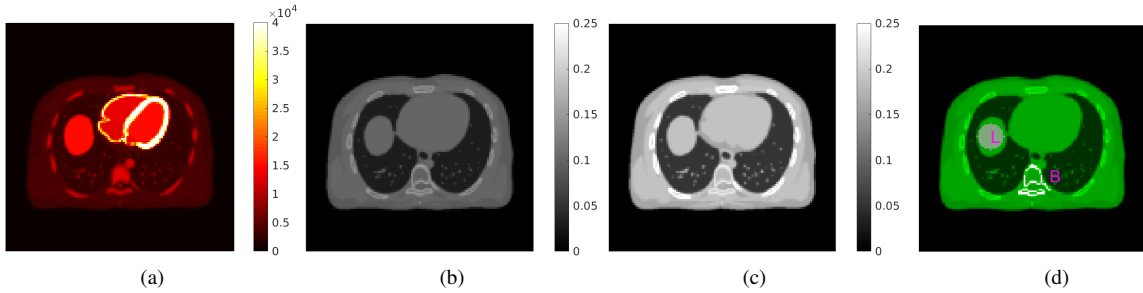


Fig. 3: The digital phantom used in the PET/CT computer simulation. (a) PET activity image in Bq/cc; (b) PET attenuation image at 511 keV in cm^{-1} ; (c) X-ray CT image at 80 keV; (d) illustration of a liver ROI ‘L’ and a spine bone ROI ‘B’.

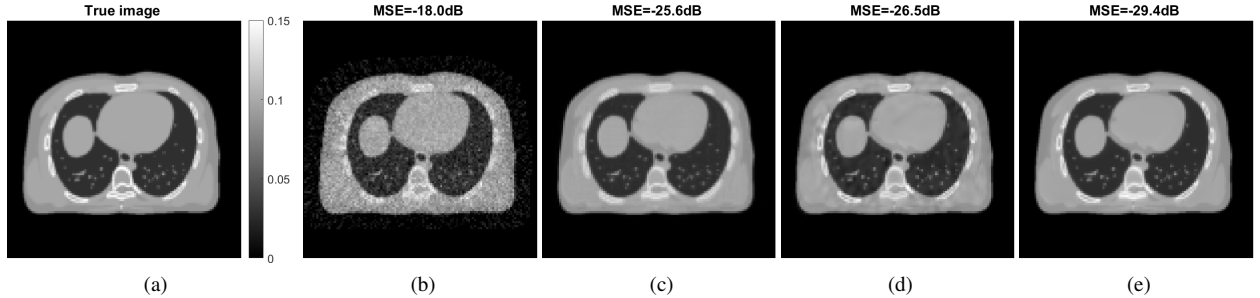


Fig. 4: gCT images by different reconstruction algorithms. (a) Ground truth, (b) MLLA, (c) KAA, (d) DIP, and (e) proposed neural KAA.

B. Compared Methods and Implementation Details

In this work, four types of reconstruction methods were compared, including (1) the standard MLLA [5], (2) existing KAA [3], (3) a DIP reconstruction method, which is equal to the proposed neural KAA with $\mathbf{K} = \mathbf{I}$, and (4) proposed neural KAA.

For constructing kernels, the feature vector \mathbf{f}_j was chosen as the pixel intensities of X-ray CT image in a 3×3 image patch centered at pixel j . The radial Gaussian kernel function, $\kappa(\mathbf{f}_j, \mathbf{f}_i) = \exp(-\|\mathbf{f}_j - \mathbf{f}_i\|^2/2\sigma^2)$, was used to build the kernel matrix \mathbf{K} using $\sigma = 1$ and k NN search with $k = 50$, in the same way as [3].

We adopted a modified residual U-Net architecture, as illustrated in Fig. 1b, for representing the gCT image. Please refer to [13], [18] for its advantages over the original U-Net model, along with the detailed network operations. The input image of the neural network in the DIP and neural KAA methods was set to the X-ray CT image, that can be explained as the conditional deep image prior [38]. We used the Adam algorithm with a learning rate of 10^{-3} and 150 iterations for the neural network learning, which was the same setting as our previous work [18]. The tomographic reconstruction step was implemented in MATLAB and the neural-network learning step was implemented in PyTorch, both on a PC with an Intel i9-9920X CPU with 64GB RAM and a NVIDIA GeForce RTX 2080Ti GPU.

The initial estimate of the PET activity image was set to a uniform image. Following [3], we used the X-ray CT-converted 511 keV attenuation map as the initial estimate of gCT image for accelerated convergence. All reconstructions were run for 3000 iterations for investigating the convergence behaviors of different algorithms.

C. Evaluation Metrics

As the focus of this work is on gCT for DECT, the evaluation of PET activity image quality is not concerned. Different reconstruction algorithms were first compared for gCT image quality using the mean squared error (MSE),

$$\text{MSE}(\hat{\boldsymbol{\mu}}) = 10 \log_{10} (\|\hat{\boldsymbol{\mu}} - \boldsymbol{\mu}^{\text{true}}\|^2 / \|\boldsymbol{\mu}^{\text{true}}\|^2) \quad (\text{dB}), \quad (44)$$

where $\hat{\boldsymbol{\mu}}$ represents the reconstructed gCT image by each method and $\boldsymbol{\mu}^{\text{true}}$ denotes the ground truth. The ensemble bias and standard deviation (SD) of the mean intensity in a regions of interest (ROI) were also calculated to evaluate ROI quantification in a liver region and a bone region (Fig. 3(d)),

$$\text{Bias} = \frac{|\bar{c} - c^{\text{true}}|}{c^{\text{true}}}, \quad \text{SD} = \frac{1}{c^{\text{true}}} \sqrt{\frac{\sum_{i=1}^{N_r} |c_i - \bar{c}|^2}{N_r - 1}}, \quad (45)$$

where c^{true} is the true average intensity in a ROI and $\bar{c} = \frac{1}{N_r} \sum_{i=1}^{N_r} c_i$ denotes the mean of N_r realizations ($N_r = 10$).

Different reconstruction algorithms were further compared for DECT multi-material decomposition. Similarly, the image MSE and ROI-based bias and SD were calculated for each of the material basis fractional images.

D. Comparison for gCT Image Quality

Fig. 4 shows the true and reconstructed 511-keV gCT images using different algorithms with 400 iterations. The image MSE results were included for quantitative comparison. The MLLA reconstruction was noisy. The KAA method substantially improved the gCT image quality, but with a lower contrast in the bone region as compared to the ground truth. The DIP method had a slightly better MSE than KAA, but it induced artifacts, which was in turn propagated into the

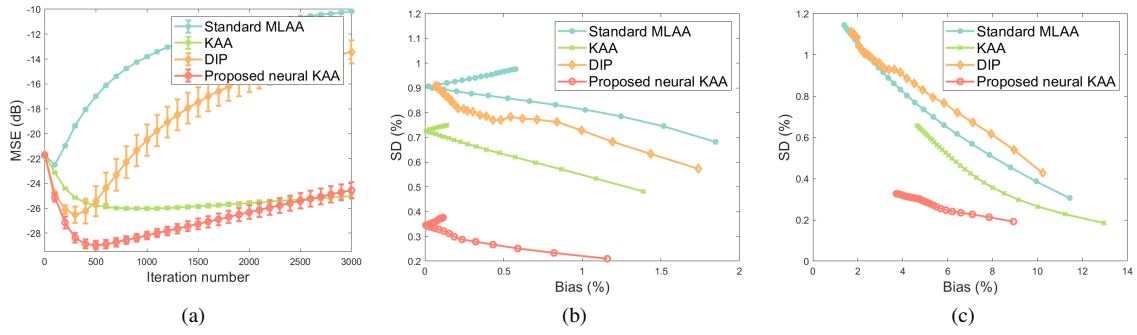


Fig. 5: Quantitative comparison of different reconstruction algorithms for gCT image quality. (a) Plot of gCT image MSE as a function of iteration number; (b-c): Plot of bias versus SD trade-off for gCT image quantification in (b) a liver ROI and (c) a bone ROI.

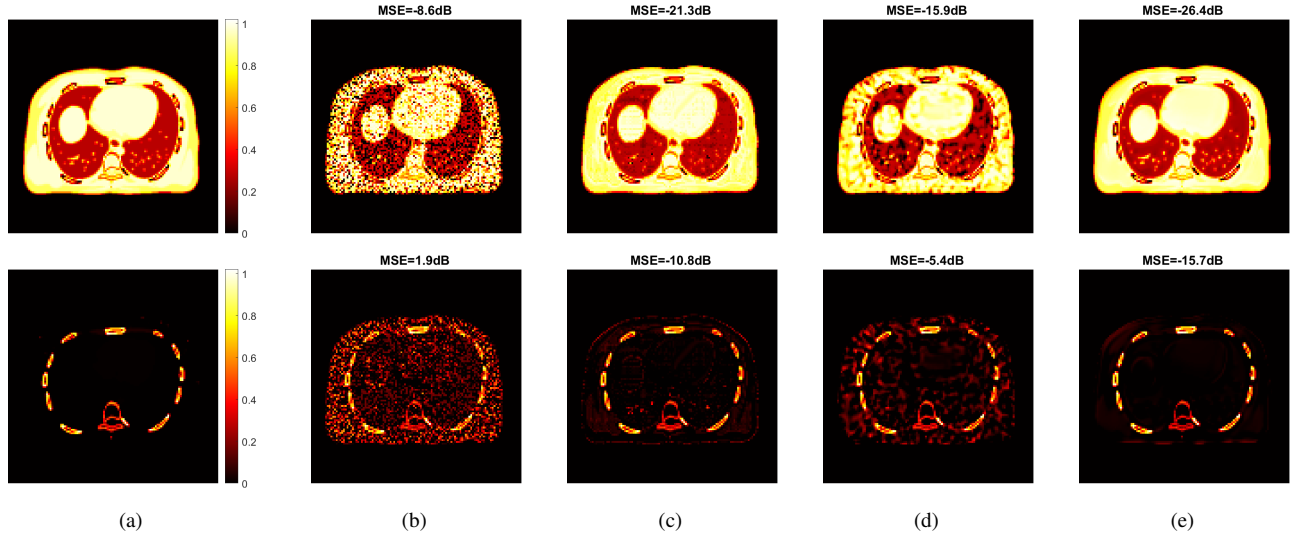


Fig. 6: True and estimated fractional images of two basis materials using different reconstruction algorithms: soft tissue (top row) and bone (bottom row). (a) Ground truth, (b) standard MLAA, (c) KAA, (d) DIP, and (e) proposed neural KAA.

material decomposition results as shown later in Fig. 6. In comparison, the proposed neural KAA demonstrated the least level of noise with good visual quality, and achieved the lowest MSE among different algorithms.

Fig. 5a shows the MSE plots as a function of iteration number for different algorithms. The iteration number varied from 0 to 3000 with a step of 100 iterations and error bars were calculated over the 10 noisy realizations. Compared to KAA, the proposed neural KAA showed a lower MSE among different methods. The curve also shows that similar to other algorithms, early stopping of the iterations is beneficial for the neural KAA to obtain good image quality while keep computational efficiency.

Fig. 5b and Fig. 5c further show the comparison of ensemble bias versus SD for gCT quantification in a liver region and a bone region. The curves were obtained by varying the iteration number from 300 to 3000 iterations with an interval of 100 iterations. As iteration number increases, the bias of ROI quantification is reduced while the SD increases. At a comparable bias level, the proposed neural KAA had a lower noise SD than the other three methods.

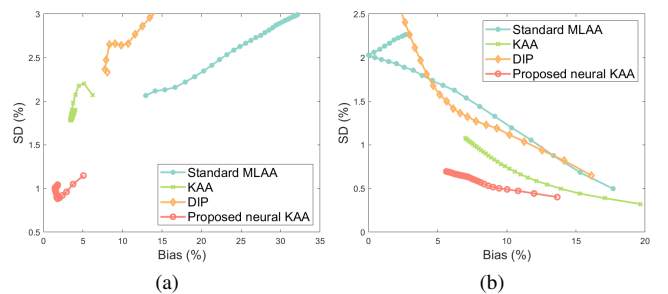


Fig. 7: Bias versus SD trade-off for ROI quantification on the fractional image of (a) soft tissue and (b) bone basis materials.

E. Comparison for Material Decomposition

We also conducted a comparison of different reconstruction methods for multi-material decomposition (MMD). Fig. 6 shows the fractional basis images of soft tissue (top row) and bone (bottom row) obtained from MMD of the PET-enabled DECT images with 400 iterations. The ground truth of the soft tissue and bone bases was generated using the noise-free pair of low-energy X-ray CT image and the 511 keV gCT image.

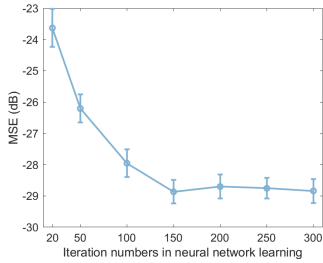


Fig. 8: Effect of iteration number of neural network learning on gCT image MSE in the neural KAA.

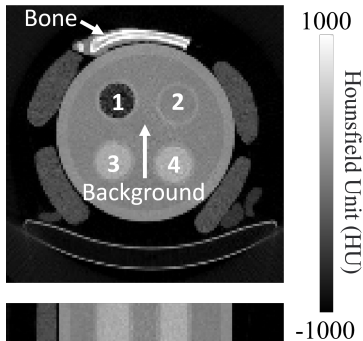


Fig. 9: Transverse (top) and coronal (bottom) slices of the 80 kVp X-ray CT image.

The conventional KAA method outperformed MLAA but were still with noise artifacts. Interestingly, even though the DIP reconstruction had a better MSE for gCT images than KAA, the benefit did not propagate into the MMD basis images. The proposed neural KAA achieved less noise and artifacts than KAA thanks to the deep image prior on the kernel coefficient image α .

Fig. 7 shows the quantitative comparisons of ensemble bias versus SD for ROI quantification on the soft tissue (a) and bone (b) fractional images by varying the reconstruction iteration number. Similar to the results of gCT ROI quantification, the neural KAA achieved the lowest noise level at a comparable bias level. It is noticeable that for the bone ROI quantification, both the standard KAA and neural KAA showed a bias when compared to MLAA. The bias was propagated from the gCT reconstruction (as shown in Fig. 5c).

F. Investigation of Neural Network Learning Settings

Our experiments indicated that neural network learning is stable when the learning rate in the Adam optimizer ranges from 10^{-4} to 10^{-2} . A larger rate may make the learning difficult to converge, while a smaller rate may reduce the convergence rate. Another important hyper-parameter is the sub-iteration number used in the network learning. Fig. 8 shows the effect of this sub-iteration number on the gCT image MSE, which suggests the MSE becomes stable after 150 subiterations.

VI. EVALUATION ON REAL PHANTOM DATA

A. Phantom Data Acquisition

We have further evaluated different reconstruction methods using a real three-dimensional (3D) phantom scan on the uEX-

PLORER PET/CT scanner [39] at UC Davis. This phantom [41] was filled with water in the background and four inserts were filled with (1) lung tissue equivalent material, (2) water, and (3&4) salt water, as shown in Fig. 9. Other attenuation materials composed of fat tissue-equivalent materials and bovine rib bones were wrapped around the phantom. A ^{18}F -FDG solution was uniformly filled in all five compartments. Two X-ray CT scans, one at 80 kVp and the other at 140 kVp, were acquired to provide the reference for MMD analysis. In this study, the reconstructions were performed on a truncated dataset of 2-min scan duration and 7 cm axial length to reduce computational time. The reconstructed gCT image size was $150 \times 150 \times 17$ with a voxel size of $4 \times 4 \times 4 \text{ mm}^3$.

B. Reconstruction Methods

We used the 80 kVp CT image as the image prior to generate the kernel matrix K and the input of the neural network. The settings of the neural network in the DIP method and proposed neural KAA were the same as in the simulation study except using a 3D version of U-Net to match with the data. All reconstructions were implemented using the CASToR package [40] as described in [41] and run for 400 iterations. The 80 kVp X-ray CT-converted attenuation map was used as the initial for gCT.

C. Results

Fig. 10 shows the gCT images reconstructed using different algorithms with 400 iterations. Similar to the results shown in the simulation, the MLAA was extremely noisy. Both the standard KAA and DIP methods reduced noise significantly but still contained significant artifacts. In contrast, the proposed neural KAA demonstrated the best visual quality.

Fig. 11 shows the bone fractional images from MMD using different approaches. Compared to the reference from X-ray DECT, the image by MLAA demonstrated heavy noise. Both the KAA and DIP methods suppressed the noise, but not without additional noise or artifacts. In comparison, the proposed neural KAA demonstrated the least artifacts and noise in the uniform regions and achieved the most similar bone fraction pattern with the reference image, as pointed by the arrows.

Fig. 12 further shows a quantitative comparison for ROI quantification of bone fraction. Here the ROI quantification is plotted versus the background noise SD measured in the water region by varying the iteration number from 40 to 400 with an interval of 20 iterations. As the iteration number increases, the estimated bone fraction becomes lower while the SD increases. Compared to the other three methods, the proposed neural KAA was the closest to the X-ray DECT reference (dashed line) and also achieved the lowest background noise level.

VII. DISCUSSION

This work proposed a neural network-based solution to improve the kernel method KAA for gCT image reconstruction in PET-enabled DECT imaging. The resulting neural KAA estimates neural network parameters from PET projection data

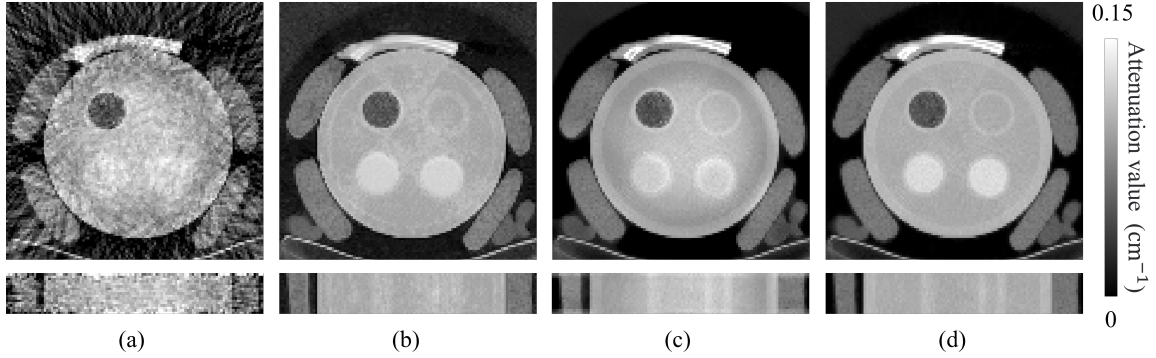


Fig. 10: Reconstructed 3D gCT images for the real phantom data using (a) MLAA, (b) KAA, (c) DIP, and (d) proposed neural KAA. Each reconstruction is shown in the transverse (top) and coronal (bottom) views.

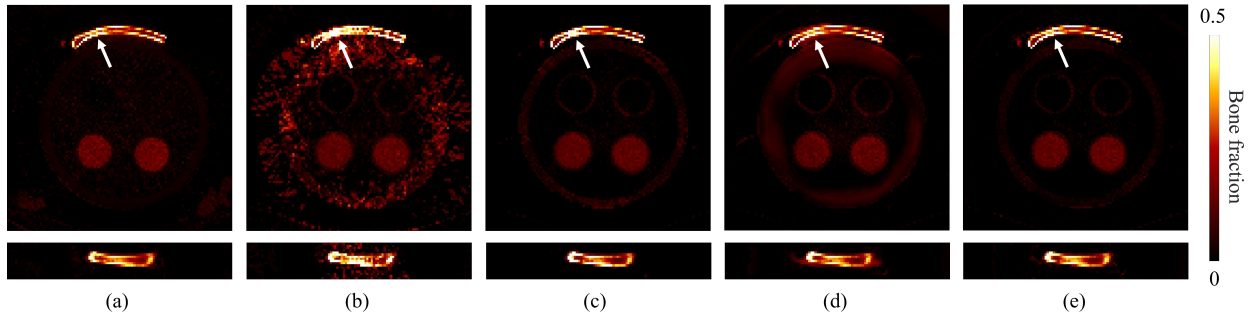


Fig. 11: Estimated bone fractional images from (a) X-ray DECT images and (b-e) PET-enabled DECT reconstructed with (b) MLAA, (c) KAA, (d) DIP, and (e) proposed neural KAA. Each 3D image is shown in the transverse (top) and coronal (bottom) views.

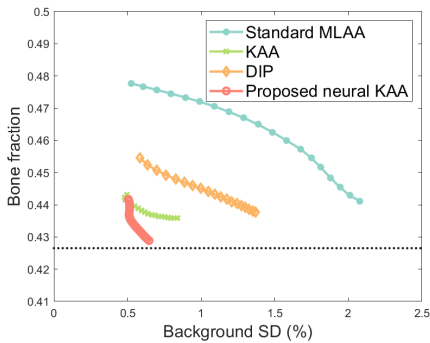


Fig. 12: Plot of bone fraction versus background noise for a bone ROI in the bone fractional image by varying iteration number from 40 to 400. Dash line denotes the bone fraction obtained from X-ray DECT-based bone basis image.

and is a challenging optimization problem. We have solved this problem by developing a neural optimization transfer algorithm, which decouples the optimization problem into modular steps that can be easily implemented using existing libraries for image-based neural network learning and projection-based tomographic reconstruction, respectively.

Another way to decouple the neural network learning step from the tomographic reconstruction step would be to use the alternating direction method of multipliers (ADMM) algorithm in a way similar to [13]. However, ADMM often involves one or more hyper-parameters that are difficult to tune. Our comparisons have indicated ADMM is less stable than the

proposed neural optimization transfer algorithm for gCT reconstruction (results not shown due to space limit), which can be also projected from our previous study comparing the neural KEM with ADMM for PET activity reconstruction [18].

Similar to many other deep learning approaches, the neural network learning module of the proposed algorithm involves hyper-parameters, such as the subiteration number and learning rate. However, these parameters were all set to be the same as we used in our other works [18]. The stable performance that we have observed indicates the robustness of the neural optimization transfer algorithm, despite the different tomographic reconstruction tasks. Future studies may continue the evaluation of the stability using more datasets.

While the proposed neural KAA method here improves gCT image reconstruction by enhancing the kernel coefficient image α , the kernel matrix \mathbf{K} itself may also be improved by using trained kernels following the deep kernel concept [42]. The combination of an improved kernel with the neural KAA method may bring additional improvements and will be investigated in future work.

VIII. CONCLUSION

In this paper, we have developed a neural KAA approach that combines the kernel method with neural network-based deep coefficient prior to improve gCT image reconstruction from PET emission data. A neural optimization transfer algorithm has been developed to address the optimization challenge. Computer simulation and real phantom results for

gCT image reconstruction and multi-material decomposition have demonstrated the feasibility of the neural KAA method and shown noticeable improvements over the existing methods for PET-enabled DECT imaging.

REFERENCES

- [1] C. H. McCollough, S. Leng, L. Yu, and J. G. Fletcher, "Dual-and multi-energy CT: principles, technical approaches, and clinical applications," *Radiology*, vol. 276, pp. 637-653, Mar. 2015.
- [2] H. Wu, Y. Fang, Y. Yang, H. Huang, X. Wu and J. Huo, "Clinical utility of dual-energy CT used as an add-on to 18F FDG PET/CT in the preoperative staging of resectable NSCLC with suspected single osteolytic metastases," *Lung Cancer*, vol. 140, pp. 80-86, Nov. 2020.
- [3] G.B. Wang, "PET-enabled dual-energy CT: image reconstruction and a proof-of-concept computer simulation study," *Phys. Med. Biol.*, vol. 65, p. 245028, Nov. 2020.
- [4] S. Li and G.B. Wang, "Modified kernel MLAA using autoencoder for PET-enabled dual-energy CT," *Philos. Trans. Royal Soc. A*, vol. 379, no. 2204, 2021.
- [5] A. Rezaei, T. B. Terzopoulos, and H. Zaidi, "Simultaneous reconstruction of activity and attenuation in time-of-flight PET," *IEEE Trans. Med. Imag.*, vol. 31, no. 12, pp. 2224-2233, Dec. 2012.
- [6] J. Nuyts, P. Dupont, S. Stroobants, *et al.*, "Simultaneous maximum a posteriori reconstruction of attenuation and activity distributions from emission sinograms," *IEEE Transactions on Medical Imaging*, 18(5): 393 - 403, 1999.
- [7] G.B. Wang and J. Qi, "PET image reconstruction using kernel method," *IEEE Trans. Med. Imag.*, vol. 34, no. 1, pp. 61-71, Jan. 2015.
- [8] G.B. Wang, "High temporal-resolution dynamic PET image reconstruction using a new spatiotemporal kernel method," *IEEE Trans. Med. Imag.*, vol. 38, no. 3, pp. 664-674, Mar. 2019.
- [9] W. Hutchcroft, G.B. Wang, K. Chen, C. Catana, and J. Qi, "Anatomically-aided PET reconstruction using the kernel method," *Phys. Med. Biol.*, vol. 61, no. 18, pp. 6668-6683, 2016.
- [10] P. Novosad and A. J. Reader, "MR-guided dynamic PET reconstruction with the kernel method and spectral temporal basis functions," *Phys. Med. Biol.*, vol. 61, no. 12, pp. 4624-4645, 2016.
- [11] J. Bland *et al.*, "MR-guided kernel EM reconstruction for reduced dose PET imaging," *IEEE Trans. Radiat. Plasma Med. Sci.*, vol. 2, no. 3, pp. 235-243, May 2018.
- [12] D. Ulyanov, A. Vedaldi, and V. Lempitsky, "Deep image prior," *Int. J. Comput. Vis.*, vol. 128, no. 7, pp. 1867-1888, 2020.
- [13] K. Gong, C. Catana, J. Y. Qi, and Q. Z. Li, "PET image reconstruction using deep image prior," *IEEE Trans. Med. Imag.*, vol. 38, no. 7, pp. 1655-1665, Jul. 2019.
- [14] K. Gong *et al.*, "Iterative PET image reconstruction using convolutional neural network representation," *IEEE Trans. Med. Imag.*, vol. 38, no. 3, pp. 675-685, Mar. 2019.
- [15] Z. Xie *et al.*, "Generative adversarial network based regularized image reconstruction for PET," *Phys. Med. Biol.*, vol. 65, no. 12, pp. 125016, 2020.
- [16] K. Ote, F. Hashimoto, Y. Onishi, T. Isobe and Y. Ouchi, "List-mode PET image reconstruction using deep image prior," *IEEE Trans. Med. Imag.*, vol. 42, no. 6, pp. 1822-1834, June 2023.
- [17] Z. Xie, T. Li, X. Zhang, W. Qi, E. Asma, and J. Qi, "Anatomically aided PET image reconstruction using deep neural networks," *Med. Phys.*, vol. 48, no. 9, pp. 5244-5258, Sep. 2021.
- [18] S. Li, K. Gong, R. D. Badawi, E. J. Kim, J. Qi and G.B. Wang, "Neural KEM: A kernel method with deep coefficient prior for PET image reconstruction," *IEEE Trans. Med. Imag.*, vol. 42, no. 3, pp. 785-796, March 2023.
- [19] D. Hwang *et al.*, "Improving the accuracy of simultaneously reconstructed activity and attenuation maps using deep learning," *J. Nucl. Med.*, vol. 59, pp. 1624-1629, Oct. 2018.
- [20] D. Hwang *et al.*, "Generation of PET attenuation map for whole-body time-of-flight 18F-FDG PET/MRI using a deep neural network trained with simultaneously reconstructed activity and attenuation maps," *J. Nucl. Med.*, vol. 60, pp. 1183-1189, 2019.
- [21] L. A. Shepp and Y. Vardi, "Maximum likelihood reconstruction for emission tomography," *IEEE Trans. Med. Imag.*, vol. MI-1, no. 2, pp. 113-122, Oct., 1982.
- [22] H. Erdogan and J. A. Fessler, "Monotonic algorithms for transmission tomography," *IEEE Trans. Med. Imag.*, vol. 18, no. 8, pp. 801-814, Aug. 1999.
- [23] V. Y. Panin, M. Aykac, and M. E. Casey, "Simultaneous reconstruction of emission activity and attenuation coefficient distribution from TOF data, acquired with external transmission source," *Phys. Med. Biol.*, vol. 58, pp. 3649-3669, 2013.
- [24] A. Bousse *et al.*, "Maximum-likelihood joint image reconstruction/motion estimation in attenuation-corrected respiratory gated PET/CT using a single attenuation map," *IEEE Trans. Med. Imag.*, vol. 35, pp. 217-228, Jan. 2016.
- [25] A. Mehranian and H. Zaidi, "Joint estimation of activity and attenuation in whole-Body TOF PET/MRI using constrained Gaussian mixture models," *IEEE Trans. Med. Imaging*, vol. 34, pp. 1808-1821, 2015.
- [26] S. Ahn *et al.*, "Joint estimation of activity and attenuation for PET using pragmatic MR-based prior: application to clinical TOF PET/MR whole-body data for FDG and non-FDG tracers," *Phys. Med. Biol.*, vol. 63, p. 045006, 2018.
- [27] M. Defrise, A. Rezaei, and J. Nuyts, "Transmission-less attenuation correction in time-of-flight PET: analysis of a discrete iterative algorithm," *Phys. Med. Biol.*, vol. 59, pp. 1073-1095, 2014.
- [28] Y. Berker and Y. S. Li, "Attenuation correction in emission tomography using the emission data a review," *Med. Phys.*, vol. 43, pp. 807-832, 2016.
- [29] D. O. Bague, J. Leuschner, and M. Schmidt, "Computed tomography reconstruction using deep image prior and learned reconstruction methods," *Inverse Problems*, vol. 36, no. 9, p. 094004, Sep. 2020.
- [30] Z. Shu and A. Entezari, "Sparse-view and limited-angle CT reconstruction with untrained networks and deep image prior," *Computer Methods and Programs in Biomedicine* vol. 226, pp. 107167-107167, Nov. 2022.
- [31] J. Yoo, K. H. Jin, H. Gupta, J. Yerly, M. Stuber and M. Unser, "Time-dependent deep image prior for dynamic MRI," *IEEE Trans. Med. Imag.*, vol. 40, no. 12, pp. 3337-3348, Dec. 2021.
- [32] G.B. Wang and J. Qi, "Generalized algorithms for direct reconstruction of parametric images from dynamic PET data," *IEEE Trans. on Med. Imag.*, vol. 28, no. 11, pp. 1717-1726, Nov. 2009.
- [33] G.B. Wang and J. Qi, "Direct estimation of kinetic parametric images for dynamic PET," *Theranostics*, vol. 3, no. 10, pp. 802-815, 2013.
- [34] K. Lange, D. R. Hunter, and I. Yang, "Optimization transfer using surrogate objective functions," *J. Comput. Graphical Stat.*, vol. 9, no. 1, pp. 1-20, 2000.
- [35] J. A. Fessler and H. Erdogan, "A paraboloidal surrogates algorithm for convergent penalized-likelihood emission image reconstruction," in *1998 IEEE Nucl. Sci. Symp. Med. Imag. Conf.*, 1998, vol. 2, pp. 1132-5.
- [36] H. Erdogan, and J. A. Fessler, "Ordered subsets algorithms for transmission tomography," *Phys. Med. Biol.*, vol. 44, no. 11, pp. 2835-51, 1999.
- [37] W. P. Segars, M. Mahesh, T. J. Beck, E. C. Frey, and B. M. Tsui, "Realistic CT simulation using the 4D XCAT phantom," *Med. Phys.* vol. 35, no. 8, pp. 3800-8, 2008.
- [38] J. Cui, K. Gong, N. Guo, K. Kim, H. Liu, and Q. Li, "Unsupervised PET Logan parametric image estimation using conditional deep image prior," *Medical Image Analysis*, vol. 80, p. 102519, 2022.
- [39] B. Spencer *et al.*, "Performance evaluation of the uEXPLORER total-body PET/CT scanner based on NEMA NU 2-2018 with additional tests to characterize PET scanners with a long axial field of view," *J. Nucl. Med.*, vol. 62, no.6, pp. 861-870, 2021
- [40] T. Merlin *et al.*, "CASToR: a generic data organization and processing code framework for multi-modal and multi-dimensional tomographic reconstruction," *Phys. Med. Biol.*, vol. 63, no. 18, p. 185005, 2018.
- [41] Y. Zhu *et al.*, "PET-enabled dual-energy CT: open-source implementation and real data validation," *IEEE Nuclear Sciences Symposium and Medical Imaging Conference*, 2022.
- [42] S. Li and G.B. Wang, "Deep kernel representation for image reconstruction in PET," *IEEE Trans. Med. Imag.*, vol. 41, no. 11, pp. 3029-3038, Nov. 2022.